Common-Path Fourier-Domain Optical Coherence Tomography in Ophthalmology Applications

Jae-Ho Han, Xuan Liu, Kang Zhang, and Jin U. Kang,
Department of Electrical and Computer Engineering
Johns Hopkins University
3400 N. Charles Street, Baltimore, MD
{jhan16, xliu35, kzhang8, jkang}@jhu.edu

Abstract—**We have demonstrated *in vivo* three-dimensional imaging and estimated localized and quantitative hemoglobin oxygen saturation (SO$_2$) of blood vessel by using a simple, easy to operate common-path Fourier-domain optical coherence tomography (OCT) system. The common-path OCT system can be easily integrated with various surgical tools and we demonstrated its usefulness by imaging outer and inner intraocular tissues such as cornea and neurosensory retinal layers as well as detecting SO$_2$ level from a chicken embryo. The system uses 800nm near infrared broadband light sources and has axial resolution as low as 3μm in air. Self-adaptive scanning mechanism with real-time surface recognition and feedback control was also applied to the probe where the scanning probe tracks the sample surface variance and effective imaging depth was largely extended to the probe's free-moving range.**

I. INTRODUCTION

Optical coherence tomography (OCT) is one optical tomography modality in which ballistic photons are detected rather than projecting the noncoherent photons having diffuse reflection or transmittance for achieving three dimensional images. OCT has unprecedented resolution compared to other imaging modalities such as ultrasound, X-ray computed tomography (CT), and Magnetic Resonance Imaging (MRI), because the axial (or longitudinal) resolution of OCT is determined by the coherence length of the source used which is inversely proportional to the source bandwidth [1].

Unlike the conventional OCT systems that use Michelson Interferometers, this work is based on common-path Fourier-domain OCT (CP-FDOCT) which we believe is the one of the simplest, most versatile three dimensional imaging technique available and allows attachment of different kinds of probes [2]. This is possible since the scanning probe provides the reference and also serves as the transceiver. This configuration allows one to use arbitrary length of probe arm and also allows different probe attachments. Moreover, it doesn't have the problem of polarization and dispersion mismatch [3]. It is known that Fourier-domain (FD) systems are simpler, faster and better than that of time-domain (TD) systems since there is no need for mechanically A-scan. CP-FDOCT can be especially useful for ophthalmic applications [4], since the fiber optic probe can easily be integrated or attached to surgical tools and directly inserted into or placed in close proximity to the ocular tissues for image acquisition and surgical navigation for *in-situ* or *in-vivo* operation. Furthermore, the level of the hemoglobin (Hb) oxygen saturation (SO$_2$) can be easily obtained by measuring Hb and HbO$_2$ induced attenuation. Specifically, the SO$_2$ level was estimated from their spectral absorption characteristics by analyzing signal spectra [5]. Using this method, other groups have measured the SO$_2$ of human blood sample *ex vivo* [6] and in retina *in vivo* [7] in real time. Current OCT systems generally suffer from very limited imaging depth range of only 1~3mm, which restricts its clinical applications when the sample surface variance exceeds the imaging depth range [8-9]. One efficient way out is to use adaptive ranging to search the sample surface and then feed the information back to adjust the coherence gate and range on the reference arm [9-10]. For a common-path OCT system, the reference and sample signals share the same path so that the reference offset can be changed directly by adjusting the distance between the fiber probe and the sample surface.

In this study, we used fiber optic probe integrated into a surgical needle to obtain 3-D images of the outer and inner structures of intraocular tissues of animal samples. Each axial scan data set is analyzed in real-time with an edge-searching algorithm to detect the highly reflective front surface of the object so that it is able to keep a fixed distance between the probe tip and the object surface. Therefore, the probe automatically tracks the sample surface variance and the effective imaging depth can be greatly extended up to the probe's free-moving range. We also introduced a simple technique that directly employs the spectroscopic characteristics in CP-FDOCT to compare the absorption at short (<800nm) and long (>800nm) wavelength range to deduce the SO$_2$ level based on the crossover behavior of Hb and HbO$_2$ absorption around 800 nm [11].

II. INTRAOCULAR TISSUE IMAGING

The experimental set-up for the intraocular tissue imaging with the CP-FDOCT is schematically shown in Fig. 1(a) where it consists of a single SLED (EXS8410-2413) with

840nm central wavelength and ~40nm spectral FWHM, which gives a theoretical in-air resolution of ~8μm. A fiber optic directional coupler for the beam splitting and coupling, a fiber OCT probe, and a CCD-based high-speed optical spectrometer (Ocean Optics HR-4000) with a CCD detector array with 3648 pixels and 699nm~891nm range were used for the CP-FDOCT. The integrated needle probe contains a bare single mode fiber for 800nm application (the number aperture of the fiber is 0.14) where it has a core size of ~5.6μm and outer polymer buffer diameter of ~245μm and it is inserted to a 1-½″-long 25-gauge hypodermic surgical needle. For imaging the cornea, the subject eye was place vertically to mimic the real operation situation. However, in order to reduce the strong surface reflection and to increase the penetration depth, we put the eye sample into the 0.9% NaCl solution in which the refractive index is similar to that of the water, 1.33. Fig. 1(b) is the magnified microscope image of the surgical needle with the integrated fiber optic OCT probe where the diameters of the needle and fiber are 500μm and 126μm, respectively.
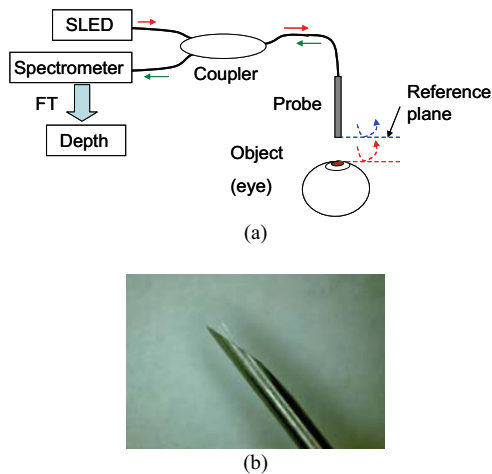

Fig. 1. Configuration of common-path Fourier-domain optical coherence tomography for eye imaging with incorporating reference plane: (a) experimental setup for intraocular tissue imaging; (b) OCT fiber probe integrated surgical needle (prototype)

The specimens we used were Spirinchus lanceolatus (or simply Shishamo) fish and Engraulis japonicus (or simply anchovy) fish. For the lateral scans (B-scan and C-scan), the probe was fixed to the two-dimensional linear stage with stepper motors in x and y -axes and have high accuracy of resolution (step size lies in 1~5μm). The measured depth or axial resolution in the A-mode scan matched well with the theoretical resolution determined by the source wavelength and its spectral bandwidth. With an eye of *Spirinchus lanceolatus*, we performed two dimensional scans of the cornea with 2μm steps in which a relatively thick anterior chamber (index ~ 1.336), a broad pupil or lens, and the iris at the edge can be observed in Fig. 2(a). Then, we performed 3D scan on an eye of *Engraulis japonicus*, with both B-scan and

C-scan steps of 5μm. Fig. 2(b) displays the 3D volume of 2000μm × 2000μm ×860μm, and Fig. 3(c) is *en face* image reconstructed from the volume data at depth =150μm from the top of Cornea. The retinal layers have their own complex characteristic reflectivity as a result of the horizontal pathways of nerve fiber layer, the neuronal cell bodies, plexiform layers of synapses, nuclear layers of additional cell bodies, and photoreceptors that comprise the retina. These structures are expressed by numerous peaks in Fig. 2(d) where pathological depth or thickness information is used for diagnosis purposes.
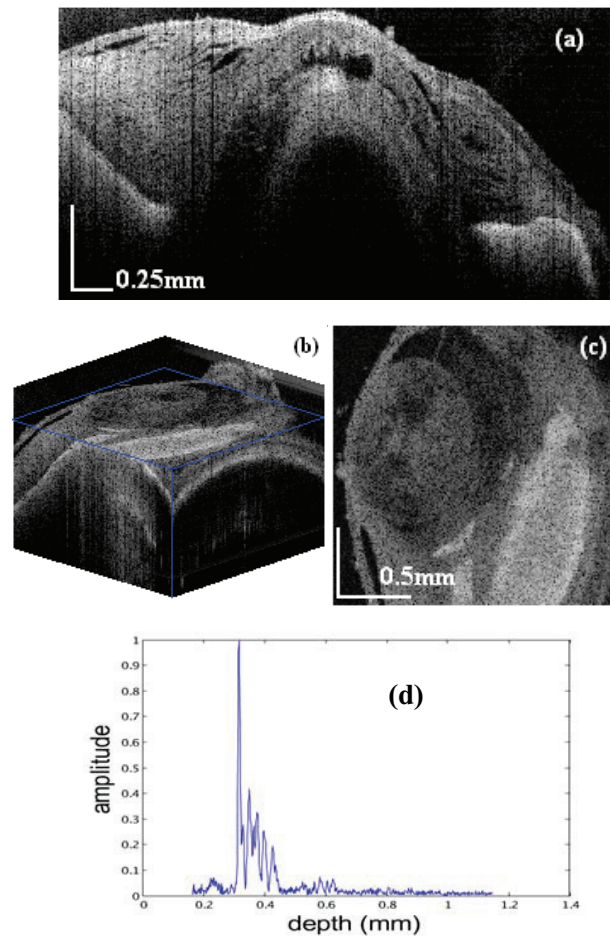

Fig. 2. Scanned OCT Images of intraocular tissues: (a) Cornea (2-D, Spirinchus lanceolatus); (b) Cornea (3-D, Engraulis japonicus); (c) Cornea *en face* image reconstructed from (b) at depth=150μm; (d) Retina (1-D, Spirinchus lanceolatus)

III. SELF-ADAPTIVE CP-FDOCT

The images obtained in the previous section used self-adoptive technique and this aspect of set-up is schematic detailed in Fig. 3(a) where a right-angle cleaved fiber probe P is maintained on a controllable 3-D moving stage M, with A-scan (axial) in X direction and B-scan (lateral) in Y direction. The reference signal comes from the Fresnel reflection at the fiber probe end, and the sample signal and the

reference are received by H, the Ocean Optics HR-4000 spectrometer. The A-scan signals are processed by the computer which then sends the control signal to M through GPIB interface.
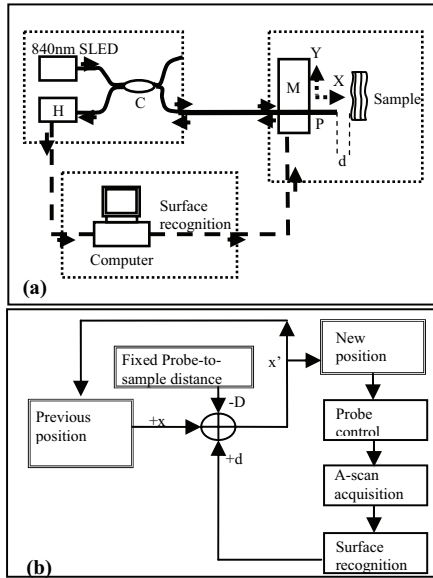

Fig. 3 Self-adaptive CP-FDOCT system:
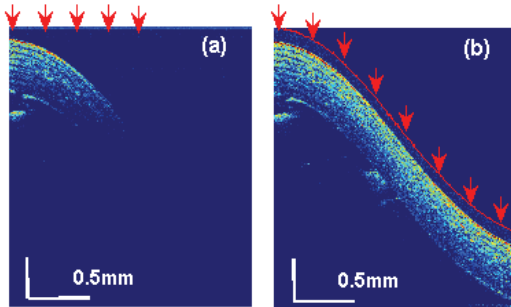(a) Experimental setup; (b) System flow chart.

Fig. 4 OCT Images of a phantom sample:
(a) Fixed-reference; (b) Self-adaptive-reference.

Fig. 3(b) shows the system flowchart. The probe is required to keep a fixed distance D from the sample surface, and in the experiment we set D=200□m. After each A-scan, the signal collected through H is processed by the computer with the edge-searching algorithm, which finds the position of the first non-noise peak. The real distance from the probe end and the sample surface is determined to be d. The new probe position is thus given by x'=x-D+d, and then the computer sent corresponding controlling command to M to adjust the probe axial position before the next A-scan. In this way the probe can keep the distance D by tracking the surface variance of the sample. The probe position for each A-scan is saved and used to reconstruct the correct image from raw data after a complete B-scan.

Using a phantom sample with 8-layers of highly curved surfaces, we first obtained a B-scan 2-D image by conventional fixed-reference method, shown as Fig. 4(a). The lateral scanning range is 2mm with a 5□m step size. The red arrows indicate the motion of the probe as well as its position. As one can see from the left part of Fig. 4(a), the CP-FDOCT has an effective working depth ~1mm and the layer structure on the "hill top" is very clear within this range. However, as expected due to the limited depth scanning range, the OCT image fades away as the probe is moved away from the top. Fig. 4(b) shows an improved image using the self-adaptive-reference method. As shown by the red arrows, the probe follows the falling of the surface as it obtains A-scans. The moving trace of probe is recorded and overlapped on Fig. 4(b) in red line, and the trace is consistent with the surface profile. By using the feedback control the probe is able to track the sample surface variance and the effective imaging depth was largely extended to the probe's free-moving range. The surface location algorithm in reference [9] and [10] is based on the first and second moment calculation of the A-scan data, which depends much on the gain factor distribution inside the sample and cannot get the accurate surface position. Compared to moment calculation, edge-searching method gives much more accurate surface location and thus better for clinic applications such as interventional ophthalmic microsurgery.

IV. OXYGEN SATURATION MEASUREMENT

The basic experimental setup was similar to the one in figure 1. However, in order measure SO_2 and to obtain higher axial resolution we combined two Superluminescent Light Emitting Diodes (SLEDs), centered at 780nm and 840nm and used it as a source. Interference spectra were recorded for OCT image reconstruction and SO_2 analysis. For homogenous blood sample, the detected signal decays exponentially with the penetrating depth. The attenuation coefficient of blood sample contains scattering coefficient and absorption coefficient, which is a function of wavelength as well as a function of SO_2.

For real biological sample such as chicken embryo, the absorption coefficient varies as tissue composition changes at difference depth. SO_2 map are obtained by processing spectra measured at different lateral position. With the same data, by simply Fourier analysis, we could obtain 2D OCT image. Fig 5 is the signal processing procedure for a single A-Scan. To obtain the spectrum of interference signal from a certain depth, a Short Time Fourier Transform (STFT) is performed. We first performed Fourier transform on the interference signal $I(k)$ to obtain $i(l)$. A moving window is used to segment the complex valued $i(l)$, and then inverse Fourier transform it was performed. The result is normalized with source spectrum $|E_0(k)|^2$, which is $i_0(k,l')$, and is used to compare the different absorption spectra of Hb and HbO_2 for wavelength above and below isobestic wavelength around 800nm.

Here $R(l')$ is defined as: $R(l') = \{mean(i_0(k,l')^2)_{red} - mean(i_0(k,l')^2)_{ir\_i}\} / mean(i_0(k,l')^2)_{ir}$. mean( )$_{red}$ and mean( )$_{ir}$ indicates to take the average of $i_0(k,l')^2$ in red (740nm-767nm)

and infrared (810nm-850nm) wavelength range. In other word, the interference fringe is low-pass filtered by averaging $i_0(k,l')^2$ over a large wavelength range. $R(l')$ shows different spectral distortion for the above and below 800 nm light, which is related to SO_2.
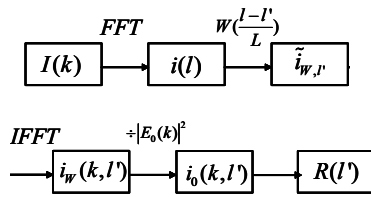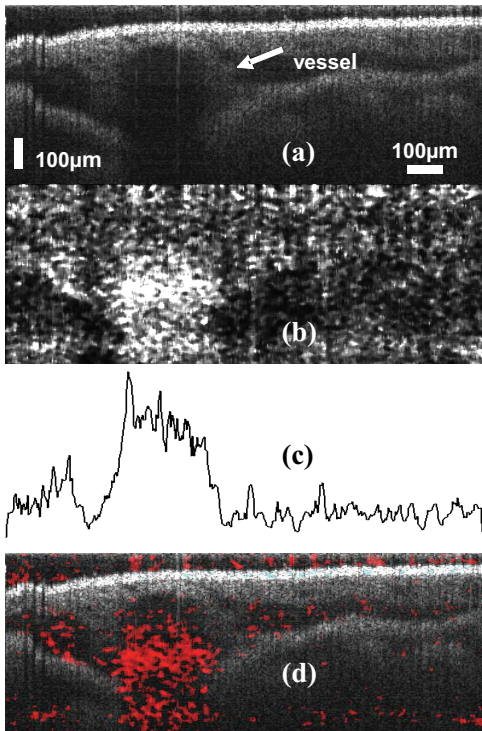

Fig. 5. Flow chart of signal processing

Fig .6. (a) OCT image (b) map of R values (c) R averaged along the axial direction (d) superimposition of OCT image and SO_2 map

Fig. 6 shows the result of our experiment. Fig. 6(a) is the *in vivo* OCT image obtained by scanning the fiber optic probe above the surface of the chicken embryo, in which the blood vessel is clearly visible. Fig. 6(b) is the map of R values, showing the spatial variation of SO_2, axially and laterally. Fig. 6(c) is obtained by averaging $R(l')$ along the depth direction. The peak indicates the blood vessel and the oxygenation saturation level corresponds well with the location of the blood vessel. In Fig. 6(d), OCT image and R map are overlapped by assigning R value to the red component of the RGB image, while assigning OCT signal intensity to the green and blue components. In Fig. 6(d), the region with large R value is superimposed with the groove region beneath the blood vessel.

In standard pulse oximeters, S_pO_2 can be easily obtained from the ratio between absorption coefficients at short wavelength and long wavelength [11]. However, in our work, $R(l')$ does not directly provide this ratio. First of all, the relationship between $i_0(k,l')$ and absorption coefficient is complicated, because of the random nature of scattering events in turbid tissue. Secondly, the spectral distortion at depth l' is determined by light absorption from the end of probe to l', which is cumulative. A more sophisticated model and experimental calibration to convert R value to actual SO_2, nevertheless the technique is effective in identifying the blood vessels and gives relative value of the SO_2 level in tissue.

V. CONCLUSION

We have demonstrated surface-tracking functional CP-FDOCT that can obtain high resolution three-dimensional images, estimated the level of oxygen saturation in the blood vessel and the blood vessel location for potential use in micro neurosensory retinal and corneal surgeries. The probe can be inserted into surgical tools for use in intra-ocular and intra-vitreous environment for image acquisition and surgical navigation.

REFERENCES

[1] A. B. Vakhtin, D. J. Kane, W. R. Wood, and K. A. Peterson, "Common-path interferometer for frequency-domain optical coherence tomography," *Appl. Opt.*, vol. 42, pp. 6953-6958, 2003.

[2] X. Li, J.-H. Han, X. Liu, J.U. Kang, "Signal-to-noise ratio analysis of all-fiber common-path optical coherence tomography," *Appl. Opt.*, vol. 47, pp. 4833-4840, 2008.

[3] D. Levitz, L. Thrane, M. H. Frosz, P. E. Andersen, C. B. Andersen, J. Valanciunaite, J. Swartling, and P. R. Hansen, "Determination of optical scattering properties of highly-scattering media in optical coherence tomography images," *Opt. Express*, vol. 12, pp. 249-259, 2004.

[4] J. Fingler, C. Readhead, D. M. Schwartz, S. E. Fraser, "Phase-Contrast OCT Imaging of Transverse Flows in the Mouse Retina and Choroid," *Invest. Ophthalmol. Vis. Sci.* vol. 49, pp. 5055-5059, 2008.

[5] D. J. Faber, E. G. Mik, M. C. G. Aalders, T. G. van Leeuwen, "Toward assessment of blood oxygen saturation by spectroscopic optical coherence tomography", *Opt. Lett.*, vol. 30, pp. 1015-1017, 2005.

[6] C. W. Lu, C. K. Lee, M. T. Tsai, Y. M. Wang, and C. C. Yang, "Measurement of the hemoglobin oxygen saturation level with spectroscopic spectral-domain optical coherence tomography", *Opt. Lett.*, vol. 33, pp. 416-418, 2008.

[7] L. Kagemann, G. Wollstein, M. Wojtkowski, H. Ishikawa, K. A. Townsend, M. L. Gabriele, V. J. Srinivasan, J. G. Fujimoto, J. S. Schuman, "Spectral oximetry assessed with high-speed ultra-high-resolution optical coherence tomography", J. Biomed. Opt., vol. 12, pp. 041212, 2007.

[8] A. Low, G. Tearney, B. Bouma, and I. Jang, "Technology insight: optical coherence tomography—current status and future development," *Nat. Clin. Pract. Cardiovasc Med.* vol. 3, pp. 154-162 (2006).

[9] N. Iftimia, B. Bouma, J. Boer, B. Park, B. Cense, and G. Tearney, "Adaptive ranging for optical coherence tomography," *Opt. Express*, vol. 12, pp. 4025-4034, 2004.

[10] G. Maguluri, M. Mujat, B. Park, K. Kim, W. Sun, N. Iftimia, R. Ferguson, D. Hammer, T. Chen, and J. Boer, "Three dimensional tracking for volumetric spectral-domain optical coherence tomography," *Opt. Express*, vol. 15, pp. 16808-16817, 2007.

[11] V. Kamat, "Pulse Oximetry", *Indian J. Anaesh*, vol. 46, pp. 261-268, 2002.